▎Microporous Materials

Systematic Investigation of the Effect of Polymerization Routes on the Gas-Sorption Properties of Nanoporous Azobenzene Polymers

Onur Buyukcakir,[a] Sang Hyun Je,[a] Joonho Park,[a] Hasmukh A. Patel,[a] Yousung Jung,[a, b] Cafer T. Yavuz,*[a, b] and Ali Coskun*[a, b]

Abstract: Functional-group-oriented polymerization strategies have contributed significantly to the initial development of porous polymers and have led to the utilization of several well-known organic transformations in the synthesis of these polymers. Because there are multiple polymerization routes that can be used to introduce the same chemical functionality, it is very important to demonstrate the effect of different polymerization routes on the gas-sorption properties of these chemically similar polymers. Herein, we have studied the rich chemistry of azobenzenes and synthesized four chemically similar nanoporous azobenzene polymers (NABs) with surface areas of up to 1021 $m^2 g^{-1}$. The polymerization routes have a significant impact on the pore-size distributions of the NABs, which directly affects the temperature dependence of the CO_2/N_2 selectivity. A pore-width maximum of 6–8 Å, narrow pore-size distribution, and small particle size (20–30 nm) were very critical for high CO_2/N_2 selectivity and N_2 phobicity, which is associated with azo linkages and realized at warm temperatures. Our findings collectively suggest that an investigation of different polymerization routes for the same chemical functionalization is critical to understand fully the combined effect of textural properties, local environment, and chemical functionalization on the gas-sorption properties of nanoporous polymers.

Introduction

Facile synthetic pathways, high thermal and chemical stabilities, and the hierarchical porosity of nanoporous polymeric materials has attracted much attention in recent years because of the wide range of applications of these polymers, such as CO_2 capture and storage, catalysis, sensors, charge carriers, and many others.[1] Emissions of CO_2 into the atmosphere account for more than half of the greenhouse gases globally, thus it is very important to develop efficient, cost-effective capture technologies to minimize the environmental impact of this gas.[1a, 2] Recent findings indicate that climate change arising from CO_2 emissions into the atmosphere has started to impact crops[3] and also has led to increasing ocean acidification, with an unprecedented record value in the past 65 million years, mainly due to the uptake of atmospheric CO_2. One of the major limi-

tations for the large-scale deployment of carbon-capture and sequestration (CCS) technologies, especially in power plants that use fossil fuels, is the cost of these systems. Moreover, there has been no real market for the captured CO_2, which has further limited the implementation of these relatively expensive technologies. In recent years, however, enhanced oil recovery from depleted oil reservoirs by using supercritical CO_2 has emerged as an important driver for the development of CCS systems[4] because this technology can potentially generate a market for the captured CO_2 in fossil-fuel-fired power plants. Moreover, some of the CO_2 used in this process is expected to remain and be stored in underground reservoirs, thus helping to reduce CO_2 emissions while creating an incentive for further CCS research. Current ethanolic amine-scrubbing technologies for CO_2 capture is problematic due to the high-energy penalty associated with the release of captured CO_2 along with the degradation of amines and their corrosive effects.[2c, 5] One way to address these issues is to resort to physisorption rather than chemisorption for postcombustion CO_2 capture. In the design of solid sorbents for CCS technologies, there are four fundamental requirements: 1) reversible uptake and release with a low-energy penalty, 2) thermal and water stability, 3) high gas selectivity at warm temperatures (ca. 40 °C), and 4) low cost. Nanoporous organic polymers[6] have emerged in recent years as promising solid sorbents for postcombustion CO_2 capture because these polymers can potentially fulfill these four requirements.

To date, several crystalline and amorphous nanoporous polymers that incorporate various chemical functionalities by using different polymerization routes (e.g., Yamamoto, Ullmann,

[a] Dr. O. Buyukcakir,⁺ S. H. Je,⁺ Dr. J. Park, Dr. H. A. Patel, Prof. Y. Jung, Prof. C. T. Yavuz, Prof. A. Coskun
Graduate School of EEWS
Korea Advanced Institute of Science and Technology (KAIST)
Daejeon 305-701 (Republic of Korea)
Fax: (+82) 42-350-2248
E-mail: yavuz@kaist.ac.kr
        coskun@kaist.ac.kr

[b] Prof. Y. Jung, Prof. C. T. Yavuz, Prof. A. Coskun
Department of Chemistry
Korea Advanced Institute of Science and Technology (KAIST)
Daejeon 305-701 (Republic of Korea)

[⁺] These authors contributed equally to this work.

Supporting information for this article is available on the WWW under http://dx.doi.org/10.1002/chem.201501233.

Suzuki, Buchwald–Hartwig, and Sonogashira–Hagihara couplings; "click" chemistry; and various condensation polymerization reactions[2b,6c,7] have been reported for efficient CO_2 capture and separation.[2b,8] None of these reports, however, investigated the effect of different polymerization routes on the gas-sorption properties of porous polymers with the same chemical functionalization. Because different polymerization routes for the same chemical functionality will offer different reactive intermediates in the synthesis of nanoporous polymers and lead to completely different morphologies, surface areas, and pore structures, the gas uptakes and selectivities of these polymers could be different, although they all will be chemically similar. Thus, it is very important to investigate the combined effect of textural properties, local environment, and chemical functionalization on the gas-sorption properties of nanoporous polymers in the design of efficient sorbents. Recently, Cooper and co-workers[9] demonstrated the effect of solvent in the synthesis of conjugated microporous polymers (CMPs) and concluded that there is no "universal" solvent for the synthesis of CMPs to obtain high surface areas and pore volumes. A similar situation was observed for clicked porous polymers synthesized through a 1,3-dipolar cycloaddition reaction. The initial report by Cooper and co-workers,[9] followed by a more detailed study by Farha and co-workers,[10] that demonstrated that the surface areas, pore volumes, and gas-uptake properties of these polymers could be significantly altered by varying the solvent, temperature, and catalyst loading. Because there are several different polymerization routes that could lead to the same chemical functionality, there is no "ideal" polymerization route for the synthesis of nanoporous polymers, thus different polymerization routes should be investigated, where possible, to understand the effect of chemical functionalization fully and to control the surface area for desired applications. We have recently developed azo covalent

organic polymers (azo-COPs) and discovered that these polymers are "N_2 phobic" and show increasing CO_2/N_2 selectivity with rising temperature mainly due to the entropic loss of N_2 molecules upon their interaction with the azobenzene moieties.[8k,11] The rich chemistry of azobenzenes prompted us to investigate further the effect of polymerization routes on the gas-sorption properties of nanoporous azobenzene polymers (NABs).

Herein, we have investigated four different polymerization routes to give NAB-1–NAB-4, respectively; that is, catalyst-free asymmetric azo coupling under basic conditions (NAB-1), copper-catalyzed oxidative azo-coupling (NAB-2), In(OTf)$_3$/Et$_3$SiH-catalyzed reductive coupling (NAB-3), and finally metal-free tert-butyl hypochlorite (tBuOCl)/NaI-catalyzed oxidative dimerization reactions (NAB-4; Scheme 1). We found that although Cu-catalyzed polymerization reactions give broad pore-size distributions, NAB-1, NAB-3, and NAB-4 had very narrow distributions that directly affect the temperature dependence of the CO_2/N_2 selectivity. Interestingly, pore-width maxima in the range 6–8 Å were very critical for high CO_2/N_2 selectivity at warm temperatures. Moreover, the change in the selectivity was mainly driven by the loss of affinity toward N_2 for NAB-1 and NAB-3, whereas the change in selectivity for NAB-2 and NAB-4 was due to the loss of affinity toward CO_2, thus pointing to the fact that the observed selectivity change for NAB-1 and NAB-3 is a result of the N_2-phobic nature of the framework that arises from pores of 6–8 Å and a narrow pore-size distribution. It is important to note that the small particle sizes of NAB-1 and NAB-3 also contributed significantly to the increase in selectivity because smaller particles are expected to form smaller interparticle void space. These results point to an N_2-phobic effect, which is observed in the case of NAB-1 and NAB-3 and is an emergent phenomena that arises from the combination of small pore and particle sizes and the interac-
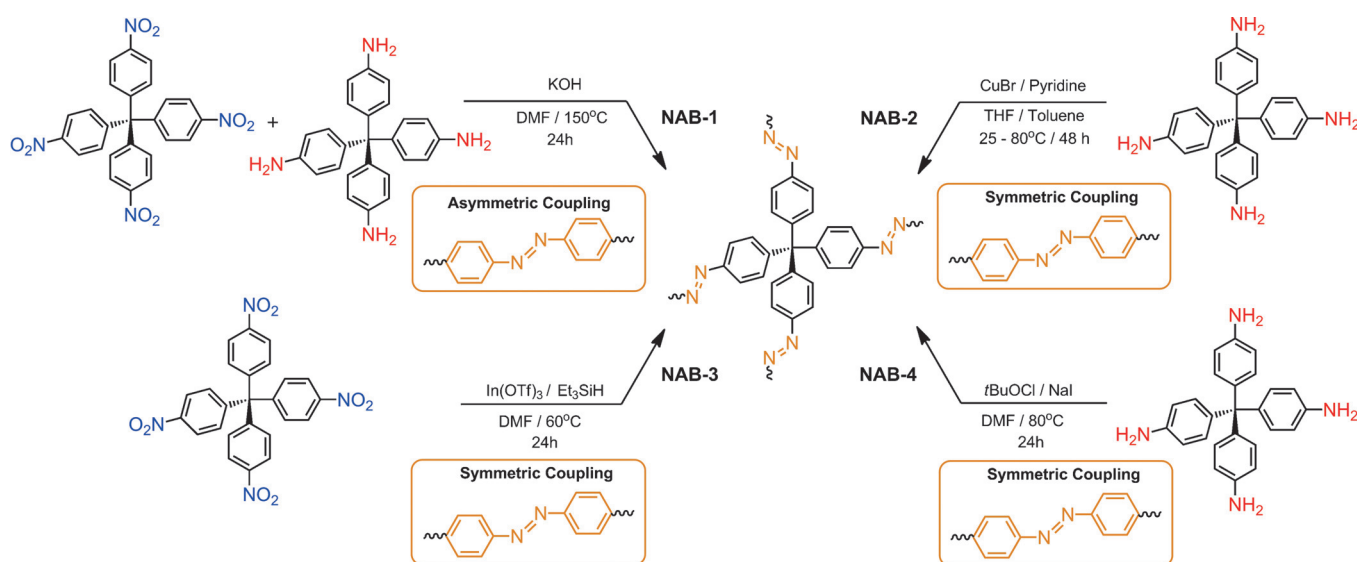
Scheme 1. Syntheses of nanoporous azobenzene polymers (NABs). A catalyst-free asymmetric coupling of tetrakis(4-nitrophenyl)methane with tetrakis(4-aminophenyl)methane in DMF at 150 °C in the presence of KOH (NAB-1); oxidative symmetric copper-catalyzed azo-coupling reaction under open-air conditions (NAB-2); In(OTf)$_3$/Et$_3$SiH-catalyzed, symmetric, reductive azo-coupling of tetrakis(4-nitrophenyl)methane (NAB-3); and metal-free tBuOCl/NaI-catalyzed (tBuOI generated in situ) oxidative dimerization of tetrakis(4-aminophenyl)methane (NAB-4) for the formation azobenzene in situ.

tion of N_2 molecules with the azobenzene units in a confined environment.

Results and Discussion

Synthetic routes assist the formation of structural features of amorphous polymeric networks. Although it is possible to use both thermodynamically and kinetically controlled reactions in the synthesis of porous polymers, a kinetically controlled pathway is generally preferred because control over porosity and pore size, even though the resulting structure is completely amorphous, is allowed. The synthesis of **NAB-1** involves the formation of a nitroso intermediate upon nucleophilic attack on the nitro oxygen atom from the amine nitrogen atom, thus leading to the elimination of a hydroxy amine derivative, which can be further converted into a nitroso functionality under basic conditions. This initial addition–elimination step could introduce some degree of thermodynamic control into the synthesis of **NAB-1**, which is followed by a fast reaction under kinetic control, that is, the coupling reaction between the nitroso and amine moieties to form azobenzene units.[12] Similarly, the synthesis of **NAB-3** also involves the formation of nitrosobenzene, thus indicating the critical role of this intermediate on the formation of narrow pores. The copper-catalyzed oxidative coupling of aromatic amines leads to the formation of **NAB-2** under kinetic control and the rate of this reaction is highly dependent on the catalyst loading. Finally, the synthesis of **NAB-4** involves a hydrogen–iodine exchange between tBuOI (generated in situ) and $ArNH_2$, thus yielding an $ArNI_2$ intermediate and subsequent elimination of HI from $ArNI_2$ and $ArNH_2$ under kinetically controlled reaction conditions. Therefore, **NAB-1**–**NAB-4** are expected to provide an ideal platform to compare the effect of different polymerization routes on the gas-sorption properties of chemically similar NABs. It is important to note that because all these polymerization routes involve different reactive intermediates and reaction kinetics, the local environment of the azobenzene units should vary drastically, which in turn should affect their gas-sorption properties to a significant extent.

The syntheses of the monomers were achieved by using previously reported procedures.[13] **NAB-1** was synthesized by coupling tetrakis(4-nitrophenyl)methane with tetrakis(4-aminophenyl)methane in the presence of KOH in an inert atmosphere. **NAB-2** was prepared by the copper(I)-catalyzed oxidative homocoupling of tetrakis(4-aminophenyl)methane.[13] **NAB-3** was obtained by reductive dimerization of tetrakis(4-nitrophenyl)methane by using $In(OTf)_3$/Et_3SiH as a catalyst in DMF at 60 °C over 24 hours.[14] **NAB-4** was synthesized by oxidative dimerization of tetrakis(4-aminophenyl)methane with tBuOI generated in situ as a catalyst in DMF at 80 °C over 24 hours.[15] The catalyst loading was critical for the metal-catalyzed reactions to control the surface area and pore morphology.

We carried out analysis by using inductively coupled plasma mass spectrometry (ICP-MS) to verify the absence of residual metal catalysts in **NAB-2** and **NAB-3**. ICP-MS analysis of **NAB-2** and **NAB-3** revealed (see the Supporting Information) that the
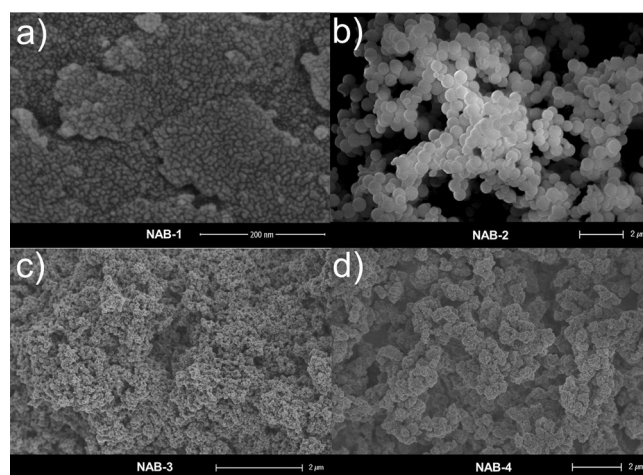
Figure 1. SEM images of NABs. a) **NAB-1** (ca. 20 nm; scale bar 200 nm), b) **NAB-2** (ca. 500 nm; scale bar 2 μm), c) **NAB-3** (ca. 25 nm; scale bar 2 μm), and d) **NAB-4** (ca. 50 nm; scale bar 2 μm).

metal contents (i.e., In, Cu) are below 0.02 wt%, thus confirming near-complete removal of metal ions following acid treatment. The NABs were characterized by using FTIR spectroscopy, solid-state magic-angle spinning ^{13}C NMR spectroscopy, powder X-ray diffraction (PXRD) studies, thermogravimetric analysis (TGA), and elemental analysis (see the Supporting Information). Characteristic azobenzene -N=N- and -C–N stretching bands were observed at $\tilde{\nu} = 1404$ and 1280 cm^{-1}, respectively, in all the NABs,[8k, 11] thus indicating the successful formation of azobenzene moieties. We also carried out field-emission scanning electron microscopy to examine the bulk-scale morphology of the NABs (Figure 1). **NAB-1** and **NAB-3** showed irregularly shaped, similarly sized particles of approximately 20 and 25 nm, respectively. On the contrary, **NAB-2** formed larger spherical particles (ca. 500 nm) with uniform particle-size distribution. We observed irregularly shaped particles in the case of **NAB-4** with a relatively broad particle-size distribution of approximately 50 nm. PXRD analysis of NABs revealed that the resulting polymers are completely amorphous (see the Supporting Information).

The porosity of NABs were evaluated by using argon adsorption–desorption isotherms at 87 K, which showed a reversible type-I isotherm and type-H4 hysteresis for the desorption for **NAB-1**, **NAB-3**, and **NAB-4**, thus indicating the presence of predominantly microporous networks (Figure 2 aisa). The surface areas were calculated by using the BET model, in which the pressure ranges were determined according to the Rouquerol plots[16] (see the Supporting Information), and were 669, 1021, 532, and 580 m^{2}g^{-1} for **NAB-1**–**NAB-4**, respectively (Table 1). The pore-size distributions were calculated from the argon adsorption isotherms by using the nonlocal DFT (NLDFT) zeolite cylindrical pore model and were in perfect agreement with the calculated isotherms (see Figure 2 b and the Supporting Information). We observed narrow pore-size distributions for **NAB-1**, **NAB-3**, and **NAB-4** with pore-width maxima of 7.1, 6.0, and 5.2 Å, respectively. **NAB-2** showed a broad pore-size distribution relative to other NABs and pore-width maxima at 5.7 Å.
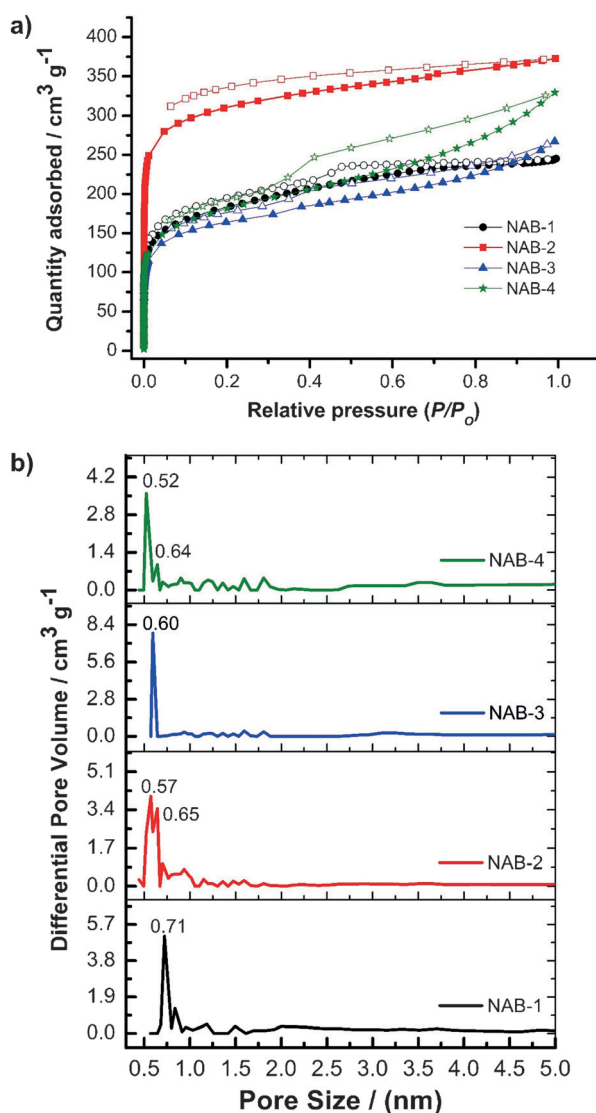
Figure 2. a) Argon-uptake isotherms of NABs at 87 K. Filled and empty symbols represent the adsorption and desorption, respectively. b) Pore-size distributions of NABs calculated by using the zeolite cylindrical pore model.

Table 1. BET and Langmuir surface areas, CO_2- and N_2-uptake capacities, CO_2/N_2 selectivities, and isoteric heats of adsorption (Q_{st}) of NABs.

NABs	BET [m² g⁻¹]	CO_2 adsorption [mg g⁻¹]			N_2 adsorption [mg g⁻¹]		CO_2/N_2 selectivity[a]		Q_{st}[b] [kJ mol⁻¹]
T [K]		273	298	323	273	298	273	298	
NAB-1[c]	669	107.6	65.3	27.4	5.9	2.4	64	96	28.6
NAB-2	1021	140.2	68.9	47.0	4.5	2.7	37	26	23.0
NAB-3	532	98.6	57.8	38.0	3.3	1.4	56	62	25.4
NAB-4	580	94.2	48.2	34.6	2.7	1.5	63	44	26.0

[a] Calculated by using IAST at a CO_2/N_2 ratio of 0.15:0.85 at 1 bar. [b] Q_{st} = isoteric heat of adsorption of CO_2 calculated from CO_2-adsorption data at 273, 298, and 323 K. [c] Gas-sorption data obtained from reference [8k].

Considering that the expected pore width for an ideal non-interpenetrated diamond network is around 21 Å,[8x] this result indicates that there is a significant degree of interpenetration in these polymers.[17]

We investigated the CO_2 and N_2 uptake of the NABs up to 1 bar at 273 and 298 K to demonstrate the effect of the polymerization routes on their gas-sorption properties (Figure 3 a,b). Also, we recorded CO_2 adsorption–desorption isotherms for NABs at 323 K (see the Supporting Information). Prior to the gas-sorption measurements, all the NABs were activated at 150 °C for 6 hours. This activation step was expected to thermally isomerize any *cis*-azobenzene unit back to its *trans* configuration and remove trapped gases and moisture.[11] **NAB-2** showed the highest CO_2-uptake capacity of 140.2 mg g⁻¹ at 1 bar and 273 K, presumably due to its higher surface area relative to the other NABs. **NAB-1** showed a CO_2-uptake capacity of 107.6 mg g⁻¹ at 1 bar and 273 K. **NAB-3** and **NAB-4** showed similar CO_2-uptake capacities of 98.6 and 94.2 mg g⁻¹ at 1 bar and 273 K, respectively. These values are lower relative to **NAB-1** and **NAB-2** due to the lower surface areas of **NAB-3** and **NAB-4**. The high CO_2 affinity of NABs originates from the -N≡N- linkage, which can interact with CO_2 molecules through dipole-quadruple interactions, wherein the azo group acts like a Lewis base and CO_2 as a Lewis acid. As expected, the CO_2-uptake capacities of all NABs decreased with rising temperature. We obtained CO_2-uptake capacities of 65.3, 68.9, 57.8, and 48.2 mg g⁻¹ at 1 bar and 298 K for **NAB-1**–**NAB-4**, respectively. We also calculated the isoteric heat of adsorption (Q_{st}) of CO_2 from the adsorption data at 273, 298, and 323 K (Figure 3c).[6b, 8k] The Q_{st} values of CO_2 for the NABs range from 23.0 to 28.6 kJ mol⁻¹ at high loadings, which are comparable to reported electron-rich polymeric networks[8o, 11, 13, 18] and suitable for postcombustion CO_2 capture because the desorption of CO_2 will be facilitated without a significant energy penalty. The Q_{st} value for **NAB-1** at high loadings was 28.6 kJ mol⁻¹, whereas it was 23.0 kJ mol⁻¹ for **NAB-2**, although both polymers have similar chemical structures. Because the surface area of **NAB-1** is significantly lower than **NAB-2**, we believe that the higher nitrogen content and degree of interpenetration[17] in **NAB-1** led to a higher Q_{st} value. **NAB-3** and **NAB-4** showed similar Q_{st} values of 25.4 and 26.0 kJ mol⁻¹. A decrease in Q_{st} values for **NAB-3** and **NAB-4** with decreasing surface area may suggest the possibility of an optimal pore size (ca. 7 Å for **NAB-1**) for a high affinity toward CO_2 in NABs. We also investigated the dependence of Q_{st} values on the CO_2 uptake, and, as expected, a steady decrease in Q_{st} values was observed due to the fact that the binding sites will be saturated as the number of CO_2 gas molecules increase.

For postcombustion CO_2 capture, porous polymers should maintain their CO_2/N_2 selectivity at warm temperatures (>40 °C) to preferentially adsorb CO_2 over N_2. Most porous polymers reported to date,[8] however, exhibit a significant decrease in their CO_2/N_2 selectivity with rising temperature, with the exception of the recently reported azo-COPs,[8k, 11] which show increasing CO_2/N_2 selectivity with rising temperature. These polymers showed N_2-phobic behavior associated with the entropic loss of N_2 molecules upon interaction with azo linkages with rising temperatures. For true N_2-phobic be-
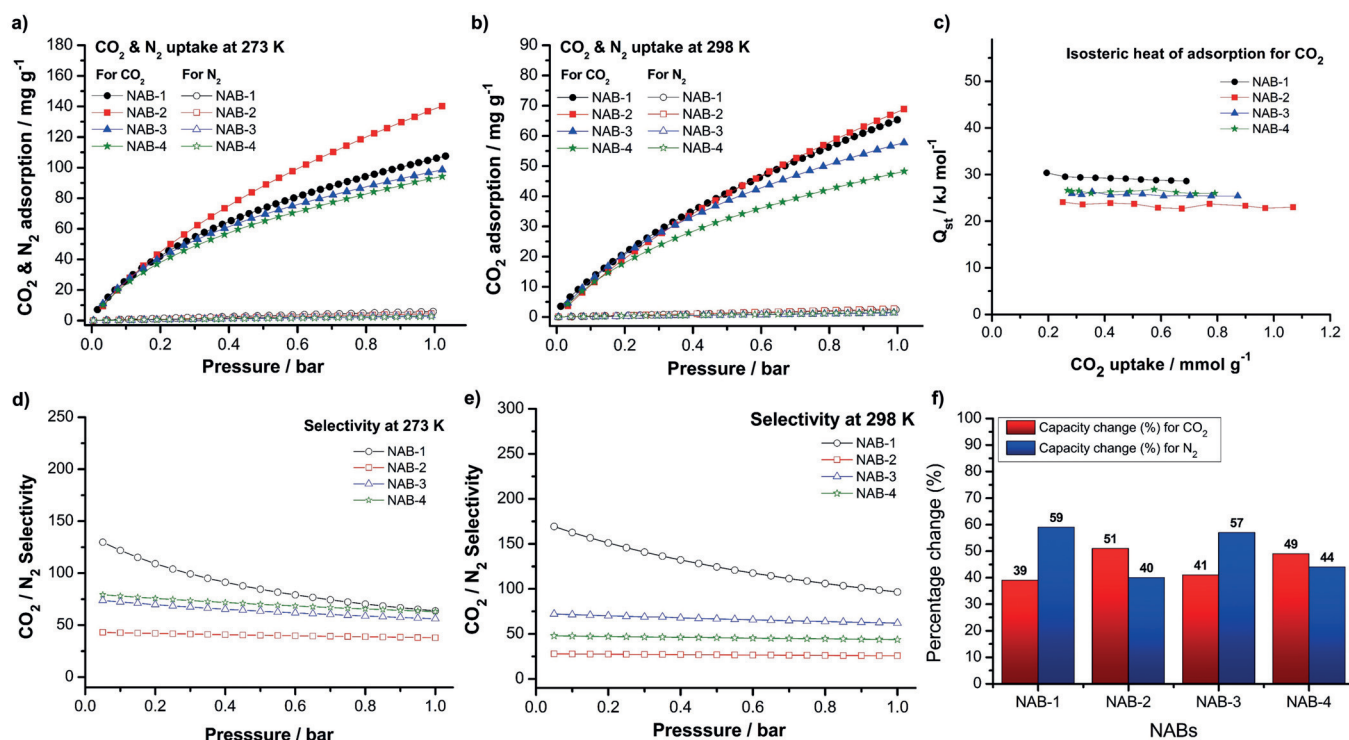
Figure 3. CO_2- and N_2-uptake isotherms of NABs measured up to 1 bar at a) 273 and b) 298 K and c) isosteric heats of adsorption (Q_{st}) of CO_2 for NABs calculated from CO_2-adsorption data at 273, 298, and 323 K. CO_2/N_2 selectivities of NABs measured by using IAST for a 15:85 molar-ratio CO_2/N_2 gas mixture at d) 273 and e) 298 K. f) Change (%) in the CO_2- and N_2-uptake capacities of NABs upon raising the temperature from 273 to 298 K at 1 bar.

havior, however, affinity loss should arise from N_2 binding, not from CO_2. One would expect to see similar N_2-phobic behavior for all of the NABs because they are all chemically similar. It is, however, important to note that the pore structures and morphologies will be completely different because NABs were synthesized by using different polymerization routes. We calculated the selectivity by using the ideal adsorbed solution theory (IAST) for a CO_2/N_2 mixture of 15:85 to simulate flue-gas conditions (Figure 3 d, e). The CO_2/N_2 selectivities for **NAB-1**–**NAB-4** were 64, 37, 56, and 63, respectively, at 273 K (Table 1). Upon increasing the temperature to 298 K, however, **NAB-1** and **NAB-3** showed an increase in their CO_2/N_2 selectivity from 64 to 96 and 56 to 62, respectively, whereas **NAB-2** and **NAB-4** showed a decrease in their CO_2/N_2 selectivities with increasing temperature. These findings prompted us to investigate the origin of the gas-capacity loss in NABs (see Figure 3 f and the Supporting Information). Upon rising the temperature from 273 to 298 K, **NAB-1** and **NAB-3** showed approximate capacity losses of 39 and 41% for CO_2 and 59 and 57% for N_2, respectively. On the contrary, **NAB-2** and **NAB-4** showed approximate capacity losses of 51 and 49% for CO_2 and 40 and 44% for N_2, respectively. These results suggest that the selectivity change of **NAB-1** and **NAB-3** was driven by the loss of affinity toward the N_2 gas molecules with rising temperature, whereas the changes in selectivity of **NAB-2** and **NAB-4** were driven by the loss of affinity toward CO_2, thus leading to a decrease in gas selectivity with increasing temperature. These results also indicate that N_2 phobicity is only present for **NAB-1** and **NAB-3**.

The differences in the change of CO_2/N_2 selectivities of NABs with increasing temperature prompted us to look into the pore-size distributions. N_2 phobicity is only observed for **NAB-1** and **NAB-3**, thus indicating that there is a critical pore-size range of 6–8 Å for N_2-phobicity to be realized. Although **NAB-2** also has pores located in the same range, its broader pore-size distribution and larger particle size (ca. 500 nm), which leads to the formation of larger interparticle void space, limits the N_2 phobic effect. Rao and co-workers[19] also reported a similar effect in metal–organic frameworks (MOFs) when they measured the N_2 uptake of MOFs containing azobenzene and stilbene moieties.[19] Interestingly, MOF-incorporating azobenzene moieties take up substantially lower N_2 gas relative to an MOF with stilbene moieties under the same conditions, thus verifying the N_2-phobic effect associated with the azo linkages. Incidentally, this MOF also has a pore aperture of 7.0 Å, which further supports a critical pore-size range for N_2 phobicity. Because the kinetic diameter of N_2 gas molecules (3.64 Å) is much smaller relative to the critical pore-size range, it is unlikely for N_2 molecules to experience a molecular-sieving effect. More recently, Lu and Zhang[20] reported the Zn-catalyzed homocoupling of tetrakis(4-aminophenyl)methane and obtained a chemically similar azo-linked porous polymer (azo-POF-1) with **NAB-1**–**NAB-4**, but with a completely different textural morphology. Although this polymer had similar surface area to **NAB-1**, its pore-width maximum was 5.4 Å and it showed affinity losses of 37 and 19% for CO_2 and N_2, respectively, thus leading to a decrease in selectivity with increasing temperature because the affinity loss is driven by CO_2. A similar situation

was also observed for the recently reported azo-linked polymers (ALPs).[13] In particular, ALP-2 has a similar chemical structure to **NAB-1**–**NAB-4**, yet with completely different gas-sorption properties, just like azo-POF-1, although the affinity loss for ALP-2 was similar for both CO_2 and N_2, these polymers exhibited pore-width maxima of 11 Å and much larger particle sizes (ca. 800 nm), thus once again verifying the importance of a critical pore-size range and particle size. These results indicate that polymers should have narrow pore-size distributions in the range 6–8 Å, small particle size (20-30 nm), and the affinity loss should be mainly driven by N_2 for N_2 phobicity to be realized.

The effect of pore size on the CO_2/N_2 selectivity can be conceptually understood by the entropy change of the gases in the adsorption process for the following two extreme cases: an infinite plane (large pores) versus a confined space (small pores; Figure 4). The Gibbs energy of adsorption can be obtained by the combination of the adsorption enthalpy and entropy; that is, $\Delta G_{ads} = \Delta H_{ads} - T\Delta S_{ads}$. When the free gases are adsorbed onto the surface, they usually lose entropy (S) due to the loss or significant reduction of translational and rotational degrees of freedom that arise from exothermic binding. Note that all the thermodynamic variables of ΔG, ΔH, and ΔS have negative values for spontaneous adsorption. Assuming a weak temperature dependence of $\Delta\Delta H_{ads}$ ($\Delta\Delta H_{ads} = \Delta H_{ads}(CO_2) - \Delta H_{ads}(N_2)$), the temperature dependence of selectivity ($\Delta\Delta G_{ads}$) is largely determined by the relative entropy changes ($\Delta\Delta S_{ads}$) during adsorption. For a usual adsorption onto a bulk surface (as an extreme of the large-pore model) in Figure 4a, the higher binding means a more rigid adsorbed complex, hence the larger loss of rotational entropy. Because CO_2 has a higher quadrupolar moment and therefore always has a higher binding energy than N_2, CO_2 will lose more entropy than N_2; that is, $|\Delta S_{ads}(CO_2)| > |\Delta S_{ads}(N_2)|$. Therefore, as the value of T increases, value of $\Delta G_{ads}(CO_2)$ rises faster ($-T\Delta S_{ads} > 0$) than the value of $\Delta G_{ads}(N_2)$ with decreased selectivity. On the other hand, when the gases are adsorbed into the confined surface of a micropore (Figure 4b), the N_2 phobicity may play a role. When N_2 is "relatively repelled" from the azo group, the space that N_2 can explore (configurational entropy) during its binding is reduced relative to the space that CO_2, which is attracted to the pore, can explore in the same pore; that is, $|\Delta S_{ads}(CO_2)| < |\Delta S_{ads}(N_2)|$ (shown schematically in Figure 4b). Based on our quantum-chemistry calculations, in fact, N_2 binds to an azo moiety with a binding energy (BE) of -8.3 kJ mol^{-1}, whereas CO_2 prefers to bind to an azo group with a BE of -16.0 kJ mol^{-1}, thus demonstrating the "N_2 phobicity of the azo group".[8k, 11] Though the intercalation would happen for a micropore in the size range 6–8 Å experimentally, **NAB-2** is shown to have larger pore-size distributions than other NABs (Figure 1). Therefore, as described above, the decrease in selectivity for **NAB-2** is typically expected, as indeed shown experimentally. For pore sizes below 6 Å, however, molecular sieving may play a role in determining the resulting CO_2/N_2 selectivity.

Conclusion

The results presented herein suggest that the selectivity increase with rising temperature is an emergent behavior that can only be realized when azo linkages are contained in small micropores (6–8 Å). The resulting polymers should also have a narrow pore-size distribution and small particle size (20–30 nm), which facilitates efficient interaction of gas molecules with azo linkages. Moreover, nanoporous polymers can be prepared to combine surface area, pore-size distribution, and desired chemical functionalities to obtain high gas selectivity and uptake by using a judicious choice of polymerization routes; thus, it is very important to investigate not only different solvents, but also different polymerization routes in the synthesis of porous polymers with the same chemical functionalization. We believe that these findings can contribute to the design of new porous polymers and allow better understanding of the role of functional groups because porous polymers with the same chemical functionalization can exhibit completely different gas-sorption properties.

Experimental Section

Materials

Starting materials and reagents were purchased from Aldrich or TCI and were used as received without further purification. Tetrakis(4-nitrophenyl)methane,[1] tetrakis(4-aminophenyl)methane,[13] and **NAB-1**[8k, 11] were prepared by following reported procedures. All reactions were performed in an argon atmosphere and dry solvents unless otherwise noted. Dry solvents were purged with argon gas before use. Analytical TLC was performed on aluminum sheets precoated with silica gel 60-F$_{254}$ (Merck 5554). Flash chromatography was carried out on silica gel 60 (Silicycle) as the stationary phase.

Synthesis of NABs

NAB-2: A modified previously reported procedure was used.[13] CuBr (25 mg, 0.174 mmol) and pyridine (107 mg, 1.35 mmol) were
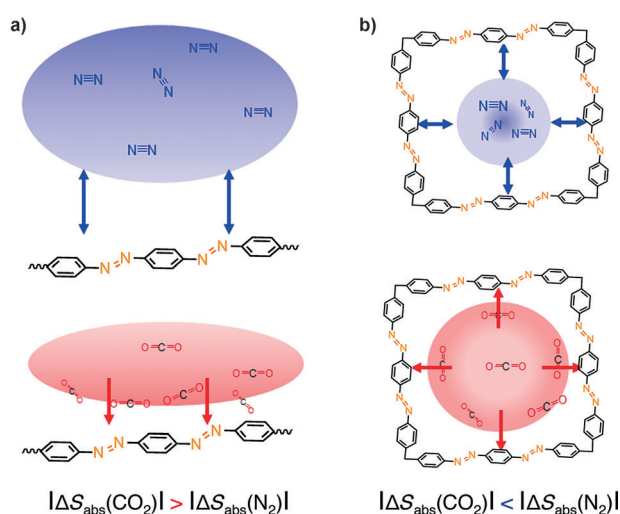
Figure 4. Schematic gas distributions of N_2 (blue) and CO_2 (red) on a) flat surface and b) micropore composed of the same functional unit.

added to a solution of tetrakis(4-aminopheyl)methane (100 mg, 0.26 mmol) dissolved in THF/toluene (1:1, 30 mL). The reaction mixture was stirred at room temperature for 24 h and then kept at 60 °C for 16 h and 80 °C for an additional 8 h. After cooling to room temperature, the reaction mixture was filtered with a fine-fritted funnel and washed with THF and water. The resulting dark-brown powder was soaked in HCl solution (2 M, 100 mL) at room temperature for 24 h before filtering. The powder was washed excessively with water, NaOH solution (1 M, 200 mL), and excessively with water, methanol, THF, acetone, and diethyl ether. The orange color solid was dried at 110 °C under vacuum for 12 h to yield **NAB-2** (82.2 mg, 85 %). Elemental analysis (%) calcd for $C_{25}H_{16}N_4$: C 80.63, H 4.33, N 15.04; found: C 71.26, H 4.43, N 10.48.

NAB-3: In(OTf)$_3$ (22 mg, 0.04 mmol) and Et$_3$SiH (0.532 mL, 3.33 mmol) were added to tetrakis(4-nitrophenyl)methane (100 mg, 0.20 mmol) dissolved in an anhydrous DMF (5 mL) in a 25 mL schlenk flask. The reaction mixture was slowly heated to 60 °C over 6 h and kept at that temperature for 24 h. The reaction was quenched with H$_2$O and soaked in 1 M HCl solution for 24 h to remove any residual metal catalyst. The precipitate was filtered and washed extensively with 1 M NaOH solution, water, THF, acetone, and diethyl ether. The orange solid was dried at 100 °C under vacuum for 12 h to yield **NAB-3** (52.0 mg, 70 %). Elemental analysis (%) calcd for $C_{25}H_{16}N_4$: C 80.63, H 4.33, N 15.04; found: C 75.26, H 4.43, N 13.46

NAB-4: *t*BuOCl (105 mg, 1.05 mmol) was added to tetrakis(4-aminopheyl)methane (50 mg, 0.13 mmol) and NaI (150 mg, 1.05 mmol) dissolved in an anhydrous DMF (5 mL) in a 10 mL schlenk flask and under argon. The reaction mixture was heated to 80 °C, kept at that temperature for 24 h, and then cooled to room temperature. The solid was separated by filtration and washed with DMF, THF, dichloromethane, acetone and diethyl ether. The dark-orange solid was dried at 100 °C under vacuum for 12 h to yield **NAB-4** (35.1 mg, 73 %). Elemental analysis (%) calcd for **NAB-4** ($C_{25}H_{16}N_4$) [found %, (calcd)] (CHN): C 80.63, H 4.33, N 15.04; found: C 76.26, H 4.43, N 12.98.

Characterization methods

^{1}H and ^{13}C NMR spectra were recorded on Bruker Avance 300 MHz NMR and Agilent 400 MHz NMR spectrometers at ambient temperature. Solid-state cross-polarization magic-angle spinning (CP/MAS) ^{13}C NMR spectra of the polymers were recorded on a Bruker Avance III 400 WB NMR spectrometer at ambient temperature with a magic-angle spinning rate of 15.0 kHz. FTIR spectra were recorded by using KBr pellets on a PerkinElmer FTIR Spectrometer. Thermogravimetric analysis (TGA) was performed on a NETZSCH-TG 209 F3 instrument, and the samples were heated to 800 °C at a rate of 10 °C min^{-1} in air and N$_2$ atmospheres. The SEM observations were carried out on a Hitachi S-4800 field-emission scanning electron microscope at 2.0–10 kV. Samples were coated with platinum prior to analysis. Elemental analysis (C, H, N) were recorded on a FlashEA 1108 (C, H, N, S) elemental analyzer. Powder X-ray diffraction (PXRD) patterns of samples were collected over the 2θ range 3–90° on a Rigaku D/MAX-2500 (18 kW) multipurpose high-power X-ray diffractometer. The measurements of the surface area and pore-size distribution of the samples were performed on a Micrometrics ASAP 2020 accelerated surface-area and porosimetry analyzer by means of argon adsorption and desorption at 87 K. The samples were degassed at 150 °C for 6 h under vacuum before the analysis. The surface areas of the samples were calculated by using the BET model in relative pressure (P/P_0) range determined according to the Rouquerol plots. The pore-size distribution of the samples was calculated by using argon isotherms according to nonlocal density functional theory (NLDFT) method, which employs the zeolite cylindrical pore model. The low-pressure CO$_2$ adsorption isotherm of the samples was obtained at three different temperatures 273, 298, and 323 K and the N$_2$ adsorption isotherms at 273 and 298 K. The circulator was used to keep the temperature constant during the adsorption analysis. The CO$_2$/N$_2$ selectivity was evaluated by using the idea adsorbed solution theory (IAST), which was calculated with OriginPro v8.5 and Mathematica v10. Heats of absorption were calculated by using standard calculation routines, that is, the Clausius–Clapeyron equation in the data-master offline data-reduction software (Micrometrics).

[1] a) D. C. Wu, F. Xu, B. Sun, R. W. Fu, H. K. He, K. Matyjaszewski, *Chem. Rev.* **2012**, *112*, 3959–4015; b) P. Kaur, J. T. Hupp, S. T. Nguyen, *Acs Catal.* **2011**, *1*, 819–835; c) S. Chandra, T. Kundu, S. Kandambeth, R. BabaRao, Y. Marathe, S. M. Kunjir, R. Banerjee, *J. Am. Chem. Soc.* **2014**, *136*, 6570–6573; d) D. Gopalakrishnan, W. R. Dichtel, *J. Am. Chem. Soc.* **2013**, *135*, 8357–8362.

[2] a) K. Sumida, D. L. Rogow, J. A. Mason, T. M. McDonald, E. D. Bloch, Z. R. Herm, T. H. Bae, J. R. Long, *Chem. Rev.* **2012**, *112*, 724–781; b) Y. H. Xu, S. B. Jin, H. Xu, A. Nagai, D. L. Jiang, *Chem. Soc. Rev.* **2013**, *42*, 8012–8031; c) D. M. D'Alessandro, B. Smit, J. R. Long, *Angew. Chem. Int. Ed.* **2010**, *49*, 6058–6082; *Angew. Chem.* **2010**, *122*, 6194–6219.

[3] a) S. S. Myers, A. Zanobetti, I. Kloog, P. Huybers, A. D. B. Leakey, A. J. Bloom, E. Carlisle, L. H. Dietterich, G. Fitzgerald, T. Hasegawa, N. M. Holbrook, R. L. Nelson, M. J. Ottman, V. Raboy, H. Sakai, K. A. Sartor, J. Schwartz, S. Seneweera, M. Tausz, Y. Usui, *Nature* **2014**, *510*, 139–142; b) M. Reyes-Fox, H. Steltzer, M. J. Trlica, G. S. McMaster, A. A. Andales, D. R. LeCain, J. A. Morgan, *Nature* **2014**, *510*, 259–262; c) R. Monastersky, *Nature* **2013**, *497*, 13–14; d) C. Mora, A. G. Frazier, R. J. Longman, R. S. Dacks, M. M. Walton, E. J. Tong, J. J. Sanchez, L. R. Kaiser, Y. O. Stender, J. M. Anderson, C. M. Ambrosino, I. Fernandez-Silva, L. M. Giuseffi, T. W. Giambelluca, *Nature* **2013**, *502*, 183–187.

[4] M. L. Godec, V. A. Kuuskraa, P. Dipietro, *Energ. Fuel.* **2013**, *27*, 4183–4189.

[5] M. Pera-Titus, *Chem. Rev.* **2014**, *114*, 1413–1492.

[6] a) D. Aaron, C. Tsouris, *Separ Sci Technol.* **2005**, *40*, 321–348; b) R. Dawson, A. I. Cooper, D. J. Adams, *Prog. Polym. Sci.* **2012**, *37*, 530–563; c) X. Feng, X. S. Ding, D. L. Jiang, *Chem. Soc. Rev.* **2012**, *41*, 6010–6022; d) N. B. McKeown, P. M. Budd, *Macromolecules* **2010**, *43*, 5163–5176.

[7] X. F. Jing, D. L. Zou, P. Cui, H. Ren, G. S. Zhu, *J. Mater. Chem. A* **2013**, *1*, 13926–13931.

[8] a) T. Ben, H. Ren, S. Q. Ma, D. P. Cao, J. H. Lan, X. F. Jing, W. C. Wang, J. Xu, F. Deng, J. M. Simmons, S. L. Qiu, G. S. Zhu, *Angew. Chem. Int. Ed.* **2009**, *48*, 9457–9460; *Angew. Chem.* **2009**, *121*, 9621–9624; b) M. Carta, R. Malpass-Evans, M. Croad, Y. Rogan, J. C. Jansen, P. Bernardo, F.

Bazzarelli, N. B. McKeown, *Science* **2013**, *339*, 303–307; c) J. W. Colson, W. R. Dichtel, *Nat. Chem.* **2013**, *5*, 453–465; d) R. Dawson, F. B. Su, H. J. Niu, C. D. Wood, J. T. A. Jones, Y. Z. Khimyak, A. I. Cooper, *Macromolecules* **2008**, *41*, 1591–1593; e) N. Y. Du, H. B. Park, G. P. Robertson, M. M. Dal-Cin, T. Visser, L. Scoles, M. D. Guiver, *Nat. Mater.* **2011**, *10*, 372–375; f) H. M. El-Kaderi, J. R. Hunt, J. L. Mendoza-Cortes, A. P. Cote, R. E. Taylor, M. O'Keeffe, O. M. Yaghi, *Science* **2007**, *316*, 268–272; g) O. K. Farha, Y. S. Bae, B. G. Hauser, A. M. Spokoyny, R. Q. Snurr, C. A. Mirkin, J. T. Hupp, *Chem. Commun.* **2010**, *46*, 1056–1058; h) A. P. Katsoulidis, M. G. Kanatzidis, *Chem. Mater.* **2012**, *24*, 471–479; i) P. Kuhn, M. Antonietti, A. Thomas, *Angew. Chem. Int. Ed.* **2008**, *47*, 3450–3453; *Angew. Chem.* **2008**, *120*, 3499–3502; j) C. F. Martín, E. Stockel, R. Clowes, D. J. Adams, A. I. Cooper, J. J. Pis, F. Rubiera, C. Pevida, *J. Mater. Chem.* **2011**, *21*, 5475–5483; k) H. A. Patel, S. H. Je, J. Park, D. P. Chen, Y. Jung, C. T. Yavuz, A. Coskun, *Nat. Commun.* **2013**, *4*, 1357; l) H. A. Patel, F. Karadas, A. Canlier, J. Park, E. Deniz, Y. Jung, M. Atilhan, C. T. Yavuz, *J. Mater. Chem.* **2012**, *22*, 8431–8437; m) H. A. Patel, C. T. Yavuz, *Chem. Commun.* **2012**, *48*, 9989–9991; n) M. G. Rabbani, H. M. El-Kaderi, *Chem. Mater.* **2011**, *23*, 1650–1653; o) M. G. Rabbani, H. M. El-Kaderi, *Chem. Mater.* **2012**, *24*, 1511–1517; p) M. Rose, W. Bohlmann, M. Sabo, S. Kaskel, *Chem. Commun.* **2008**, 2462–2464; q) M. G. Schwab, B. Fassbender, H. W. Spiess, A. Thomas, X. L. Feng, K. Mullen, *J. Am. Chem. Soc.* **2009**, *131*, 7216–7217; r) A. Thomas, *Angew. Chem. Int. Ed.* **2010**, *49*, 8328–8344; *Angew. Chem.* **2010**, *122*, 8506–8523; s) J. F. Van Humbeck, T. M. McDonald, X. F. Jing, B. M. Wiers, G. S. Zhu, J. R. Long, *J. Am. Chem. Soc.* **2014**, *136*, 2432–2440; t) S. Wan, F. Gandara, A. Asano, H. Furukawa, A. Saeki, S. K. Dey, L. Liao, M. W. Ambrogio, Y. Y. Botros, X. F. Duan, S. Seki, J. F. Stoddart, O. M. Yaghi, *Chem. Mater.* **2011**, *23*, 4094–4097; u) M. H. Weston, O. K. Farha, B. G. Hauser, J. T. Hupp, S. T. Nguyen, *Chem. Mater.* **2012**, *24*, 1292–1296; v) L. H. Xie, M. P. Suh, *Chem. Eur. J.* **2013**, *19*, 11590–11597; w) Z. G. Xie, C. Wang, K. E. deKrafft, W. B. Lin, *J. Am. Chem. Soc.* **2011**, *133*, 2056–2059; x) D. Q. Yuan, W. G. Lu, D. Zhao, H. C. Zhou, *Adv. Mater.* **2011**, *23*, 3723–3725; y) D. S. Zhang, Z. Chang, Y. B.

Lv, T. L. Hu, X. H. Bu, *Rsc Adv.* **2012**, *2*, 408–410; z) Y. L. Zhu, H. Long, W. Zhang, *Chem. Mater.* **2013**, *25*, 1630–1635.

[9] R. Dawson, A. Laybourn, Y. Z. Khimyak, D. J. Adams, A. I. Cooper, *Macromolecules* **2010**, *43*, 8524–8530.

[10] B. G. Hauser, O. K. Farha, J. Exley, J. T. Hupp, *Chem. Mater.* **2013**, *25*, 12–16.

[11] H. A. Patel, S. H. Je, J. Park, Y. Jung, A. Coskun, C. T. Yavuz, *Chem. Eur. J.* **2014**, *20*, 772–780.

[12] R. Zhao, C. Tan, Y. Xie, C. Gao, H. Liu, Y. Jiang, *Tetrahedron Lett.* **2011**, *52*, 3805–3809.

[13] P. Arab, M. G. Rabbani, A. K. Sekizkardes, T. Islamoglu, H. M. El-Kaderi, *Chem. Mater.* **2014**, *26*, 1385–1392.

[14] N. Sakai, K. Fujii, S. Nabeshima, R. Ikeda, T. Konakahara, *Chem. Commun.* **2010**, *46*, 3173–3175.

[15] Y. Takeda, S. Okumura, S. Minakata, *Angew. Chem. Int. Ed.* **2012**, *51*, 7804–7808.

[16] a) O. Buyukcakir, Y. Seo, A. Coskun, *Chem. Mater.* **2015**, *27*, 4149–4155; b) A. K. Sekizkardes, T. Islamoglu, Z. Kahveci, H. M. El-Kaderi, *J. Mater. Chem. A* **2014**, *2*, 12492–12500.

[17] W. Lu, D. Yuan, D. Zhao, C. I. Schilling, O. Plietzsch, T. Muller, S. Bräse, J. Guenther, J. Blümel, R. Krishna, Z. Li, H.-C. Zhou, *Chem. Mater.* **2010**, *22*, 5964–5972.

[18] X. Zhu, C. L. Do-Thanh, C. R. Murdock, K. M. Nelson, C. C. Tian, S. Brown, S. M. Mahurin, D. M. Jenkins, J. Hu, B. Zhao, H. L. Liu, S. Dai, *ACS Macro Lett.* **2013**, *2*, 660–663.

[19] C. M. Nagaraja, R. Haldar, T. K. Maji, C. N. R. Rao, *Cryst. Growth Des.* **2012**, *12*, 975–981.

[20] J. Lu, J. Zhang, *J. Mater. Chem. A* **2014**, *2*, 13831–13834.